

Better Localized Predictions with Out-of-Scope Information and Explainable AI: One-Shot SAR Backscatter Nowcast Framework with Data from Neighboring Region

Zhouyayan Li ^{a,b*}, Ibrahim Demir ^{a,b,c}

^a Dept. of Civil and Environmental Engineering, University of Iowa, Iowa City, Iowa, USA

^b IIHR Hydroscience and Engineering, University of Iowa, Iowa City, Iowa, USA

^c Dept. of Electrical and Computer Engineering, University of Iowa, Iowa City, Iowa, USA

* Corresponding Author, Email: zhouyayan-li@uiowa.edu

Abstract

Synthetic Aperture Radar (SAR) provides 10-m weather-independent global Earth surface observations for various tasks such as land cover land use mapping, water body delineation, and vegetation change monitoring. However, the application of SAR imagery has been limited to retrospective tasks by a “first event then observation” rule. Recent studies have proven the feasibility of a one-shot forecast of backscatters of SAR imagery using meteorological driving forces, soil moisture, geomorphic factors, and previous SAR images collected for the target area. Although the approach is promising, spatial connectivity, more specifically, the influence of the status of surrounding areas on the target location has yet to be considered. To fill that gap, this study proposed two nowcasting frameworks that can integrate precipitation and soil moisture data collected from surrounding areas through spatial aggregation (SA) and by processing spatial series (SS), respectively. The catastrophic 2019 Central US Flooding was used as a case study with the goal of predicting backscatters of SAR imagery captured during the event. The results from SA, SS, and a framework that only considers localized input (S0) are compared against each other as well as with the benchmark performance created with persistence assumption. Results show that S0, SA, and SS outperform the benchmark. In addition, considering data from neighboring areas that contribute to the target location further improves prediction accuracy. Comparing the gradients of results considering/not considering additional data indicates that neighboring data can alter the model’s attention on each feature of the localized input matrix. The difference in gradients between SA and SS indicates the way the neighboring information is integrated also matters. The methodology proposed by this study can serve as a building block for more active usage of SAR imagery in forward-looking tasks such as early flood warning and response.

Keywords: SAR, deep learning, remote sensing, image synthesis, Explainable AI

This manuscript is an EarthArXiv preprint and has been submitted for possible publication in a peer-reviewed journal. Subsequent versions of this manuscript may have slightly different content. Please feel free to contact the corresponding author for feedback.

1. Introduction

Remote sensing (RS) images serve as a great resource for Earth observation, especially for large-scale tasks and applications. The interest in utilizing RS data in flood research is rising fast especially over the past decade as more computing resources become available with optimized algorithms and techniques (Demir and Szczepanek, 2017) and more hardware becomes better at processing large datasets. Large-scale analyses not only help with depicting a better picture to describe and help understand events happened at larger regions or scales, but also contribute to generalizable conclusions that are not limited to small or special areas (Demir *et al.*, 2015).

Most of recent literature that require RS images as input are retrospective studies because RS images tell nothing about future events. For instance, for flood inundation extent mapping images obtained prior to the event can be optional depending on the method, but we will always need those captured during or after the flood (Li and Demir, 2023d; Hu and Demir, 2021). Back-looking analyses are valuable, but ahead-of-time analyses are essential in terms of supporting quick response and real-time decision-making (Alabbad *et al.*, 2022) for natural hazards (Chitwatkulsiri *et al.* 2022; Li and Demir, 2022; Piadeh *et al.* 2022). Image synthesis is the key piece for reliable ahead-of-time analyses with RS.

There was limited work done on RS data synthesis before the introduction of deep learning (DL) models. It is not only because the physics and math connecting driving forces to RS backscatter or reflectance are too complex to describe but also because of the massive computational resources required. DL models provide a novel way of explaining phenomena from the viewpoint of data rather than processes. The advancements in hardware and memory, on the other side, remove the major barrier for large data processing. To date, however, most efforts in simulating and synthesizing RS images focus on a few topics, such as forecast or nowcast of weather variables (e.g., precipitation) (Chen and Wang 2022, Tuyen *et al.* 2022), image super-resolution and downscaling (spatial enhancement) (Sit *et al.* 2023b; 2023c; Harris *et al.* 2022), image time series generation (temporal enhancement) (Requena-Mesa *et al.* 2021, Sit *et al.* 2023a), and image translation between different RS sensors (Zhu and Kelly 2021, Czerkawski *et al.* 2022, Vandal *et al.* 2022), whereas synthesizing optical / radar images that capture Earth surface characteristics has not been well studied.

For Earth surface observation synthesis, such as generating new Sentinel Aperture Radar (SAR), Landsat, and Sentinel-2 images, there are three major obstacles: 1) To be compatible with real surface observations, the synthesized data must come with a relatively high spatial resolution that usually range between 10 to 30 m rather than at the kilometer or degree level. 2) Optical / radar surface observation synthesis focuses more on describing the influence of driving forces and other relevant factors on surface characteristics. 3) Due to the trade-off between spatial and temporal resolution (Alparone *et al.* 2022, Ao *et al.* 2022), revisit period for most satellite sensors are at the day level rather than hour or minute level, which makes data synthesis through image time series generation less applicable due to insufficient training data for the model to learn from.

Li *et al.* (2022c) proposed a one-shot forecasting framework named MA-SARNet for SAR backscatter prediction. They reported that the prediction accuracy of MA-SARNet was significantly better compared to the benchmark performance. That study proved it feasible to synthesize Earth surface observations using a few contributing factors, such as precipitation and land cover. Although MA-SARNet brings satisfying synthesized SAR backscatters compared to the real observation and shows impressive generalization capacity in out-of-scope areas, the framework takes into consideration only in situ data and ignores contributing factors from neighboring areas. Based on the mechanism of many existing approaches (e.g., hydrological and simplified conceptual models) in hydro-science field, we believe that considering the driving forces (e.g., precipitation) in surrounding areas is necessary, which can contribute to better predictions for the current location.

Recently, there have been some attempts trying to blend localized data and information from surroundings. For instance, instead of doing a convolution, Fang *et al.* (2021) flattened a 3-by-3 pixel group into a 9-by-1 sequence and processed the feature sequence with LSTM to get the output corresponding to the pixel in the middle in flood susceptibility mapping. Guo *et al.* (2022) adopted different kernel sizes to enlarge the receptive field of their CNN model for urban-scale-rapid pluvial flood prediction, so that pixels in deeper layers of the model are able to “see” more pixels in shallower layers and thus can utilize features of those shallower pixels. As we can see, however, efforts into blending information coming from different image patches, which are at the target level rather than the pixel level, and still very limited. In most studies in hydro-science research field that deal with RS data, a single pixel is usually less than 100 m in both length and width (mostly no larger than 30 m), whereas an image patch often consists of thousands of pixels and the size is usually at kilometer level. Data blending at the image patch level for DL models is very different from and far more computationally demanding than blending at the pixel level, and so far, it has not been well explored.

This study will build on results and findings of the MA-SARNet study (Li *et al.*, 2022c) to explore if precipitation and soil moisture data collected in surrounding areas contribute to model performance for the current location with the goal of nowcasting the VV (vertical polarization transmitted, vertical polarization received) band of SAR images. SAR imagery is popular for hydro-science applications where cloud pollution is common, for it is external illumination independent and can see through clouds (Yang *et al.* 2020, Kong *et al.* 2022, Li *et al.* 2022a). Thanks to the advancement of data-driven methods, especially novel deep learning (DL) techniques, scientists can now extract useful information from SAR images with powerful data models in various tasks such as flood extent mapping (Aristizabal *et al.* 2020, Bosch *et al.* 2020, Li and Demir 2023, Li *et al.* 2022b), wetland delineation (Salehi *et al.* 2018), surface change monitoring and detection (Zhang *et al.* 2020, Kseňak *et al.* 2022), and object (e.g., ship) detection (Yang *et al.* 2020). The improved availability of SAR imagery will further facilitate advancements in those subdivisions and aspects. For instance, real-time and wide availability of flood extents will help understand the flood events (Haltas *et al.*, 2021), and support better

informed decision in flood preparedness, planning (Yildirim and Demir, 2022) and mitigation in resource restrained communities (Alabbad and Demir, 2022).

Contributions of this work include the following: a) proposing two approaches that can integrate information from neighboring areas and take care of the dataflow between feedforward layers, stand-alone attention modules, convolutional neural networks (CNN), and transformers; b) exploring the efficacy of adding precipitation and soil moisture information that come from surrounding locations that drain to the current one; and c) investigating how the model's performance is affected by additional data with a gradient-based Explainable Artificial Intelligence (XAI) method.

2. Study Region and Data

This study focuses on the 2019 Central US flooding events that occurred during the Spring and Summer of 2019. This event consisted of a series of floods and influenced a large portion of Missouri and Mississippi River tributaries in Nebraska, Iowa, Missouri, and South Dakota (Flanagan *et al.* 2020). Figure 1 depicts the study area that is covered by 34 SAR images captured during the 2019 Central US Floods.

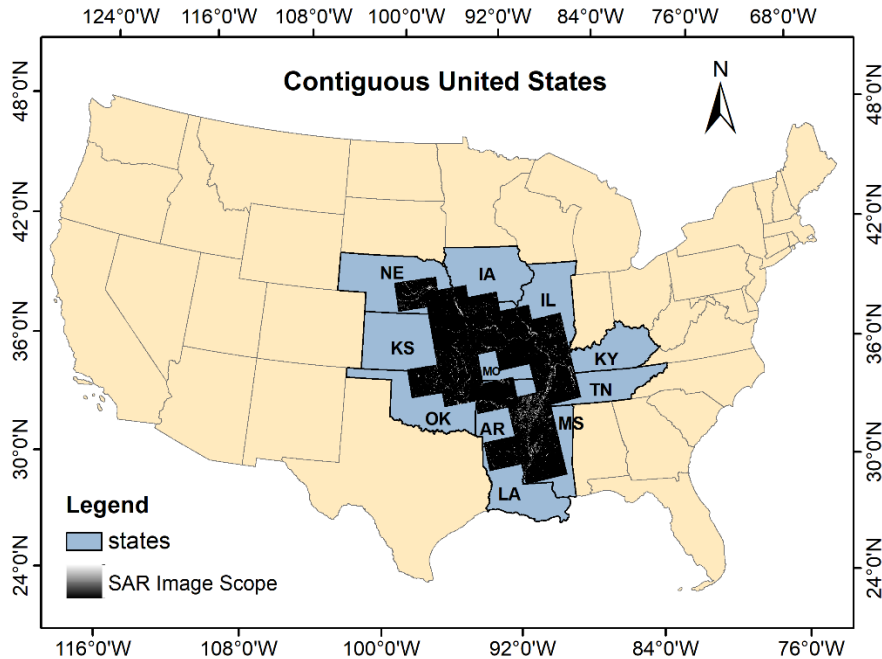


Figure 1. Study areas displayed by water body masks that are extracted from SAR images captured during the 2019 Central US Floods

The input data includes five precipitation layers, two soil moisture layers, two geomorphic layers, and one SAR image layer that is captured one revisit cycle (12 days for our case) prior to the target date for which we are predicting the SAR backscatters. Both the target and input SAR images are C-band Ground Range Detected (GRD) provided by European Space Agency (ESA)

that are openly available on Google Earth Engine (GEE). The VV band is selected out of the consideration of efficacy and computational costs, for the VV band has been reported to be more efficient compared to the VH (vertical polarization transmitted, horizontal polarization received) band especially for water body extraction (Twele *et al.* 2016, Markert *et al.* 2020, Tiwari *et al.* 2020). For simplicity, ‘SAR’ or ‘SAR images’ in following content of this paper will always be referring to the VV band of SAR images.

The five precipitation and two soil moisture layers represent rainfall and soil conditions no more than seven days prior to the target date. The precipitation data comes from the Global Precipitation Measurement (GPM) v6 product that is openly available on GEE. We aggregated the data into cumulative rainfall of 0-24h, 25-48h, 49-72h, 73-120h, and 121-168h before the timestamp of the target SAR. They will be referred to as *precip1* to *precip5* hereafter. We adopted a coarser sampling interval for the 4th to 7th days’ precipitation out of the consideration of data processing, computational costs as well as the fact that, normally, the surface situation, such as inundation status, are more sensitive to rainfall closer to the current time. The soil moisture layers come from NASA-USDA Soil Moisture Active Passive (SMAP) dataset that is also openly available on GEE. Unlike precipitation layers, soil moisture observations from SMAP are provided roughly every three days. Therefore, we selected the closest two soil moisture records prior to the target date. The soil moisture and accumulative precipitations layers are then interpolated spatially using the Kriging method to match the spatial resolution of SAR backscatters. These two soil moisture layers will be referred to as *sm1* and *sm2*, with *sm2* being the one closer to the target date.

The geomorphic inputs include a land cover map coming from EAS WorldCover 10 m 2020 V100 product (Zanaga *et al.* 2021) and a 10 m Height Above Nearest Drainage (HAND) layer created by Liu *et al.* (2016) for the continental United States. All abovementioned layers are then stacked and sliced into 256-by-256-pixel non-overlapping patches. We denote the collection containing all patches as *C0*. Finally, those patches are filtered using land cover information to remove those for which less than 10 % pixels are water bodies. This is because the backscatter of hillslope pixels will not change much compared to pixels that are located along rivers or around lake areas during meteorological processes. Therefore, including patches that contain very little water surface will be a waste of computational resources. Here, we denote the collection containing all qualified image patches as *C1*.

The USGS 3DEP 10m National Map Seamless (1/3 arc-second) DEM product pulled from GEE was used along with the D8 flow direction algorithm to determine the contributing neighbors around any target image patches. It is worth noting that the DEM data are only used for determining the contributing neighbors and are not added to the image stack. In other words, DEM data are not used as a contributing factor (feature) in the forecast. We will introduce in detail the usage of the DEM in the following section as we explain frameworks #2 and #3.

3. Model and Methodology

This section will explain the models, including the structure, component, implementation and configurations, in detail. We will also describe the XAI method used to understand those ‘black box’ structures and the indexes used to evaluate the performance of the model.

3.1. Model Structures and Configurations

As mentioned in introduction, one of the main goals of this study is to compare three nowcasting frameworks among which one only utilizes localized inputs whereas the other two take advantage of data from both the current location and neighboring areas. The two approaches considering neighboring inputs differ in the way they process and aggregate the neighboring information. Figure 2 depicts structures of those three frameworks. The bottom part (MA-NET processor) is a modified MA-Net with ResNet101 as the backbone. MA-Net was introduced by Fan *et al.* (2020) for liver and tumor segmentation. MA-Net has a U-Net structure enhanced with self-attention mechanism to blend local features and global information (Fan *et al.* 2020).

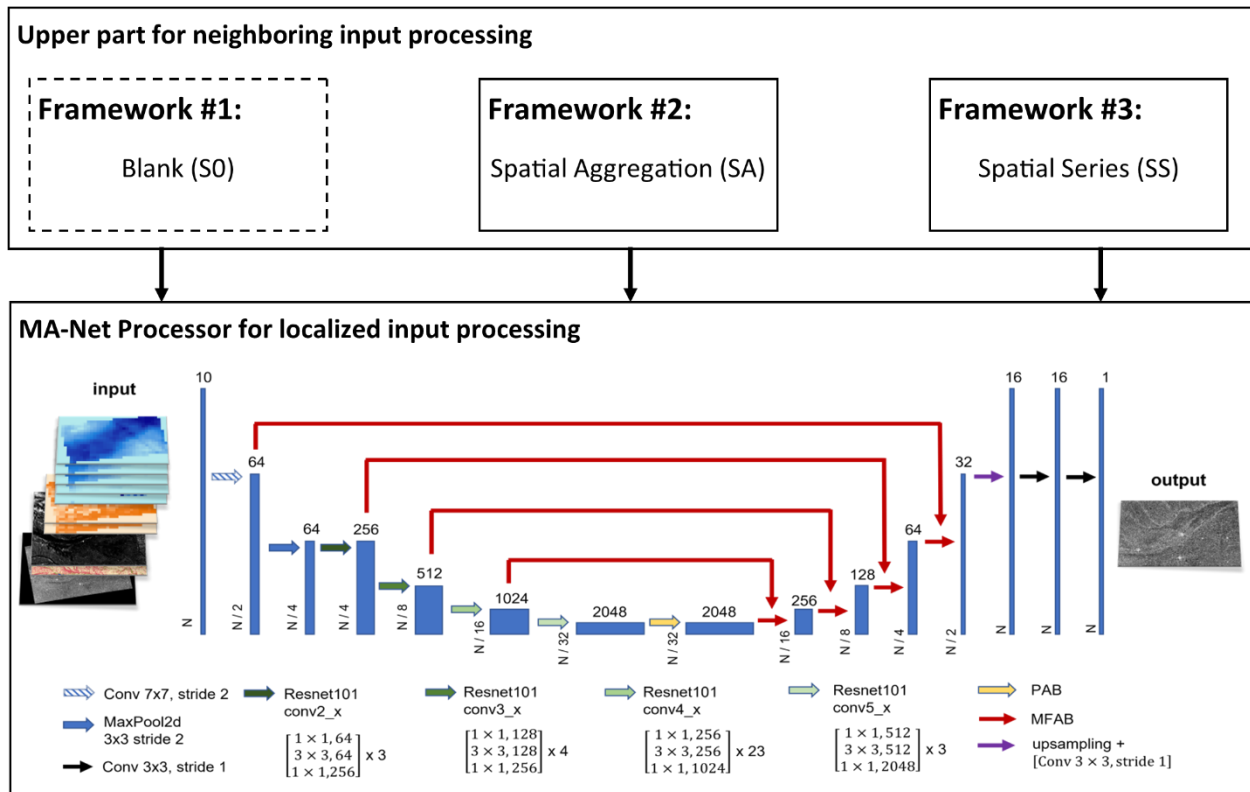


Figure 2. Structures of the three forecasting frameworks used in this study.

To make it a fair comparison, the model settings and structure for the MA-Net processor will be kept identical among all frameworks. Framework #1 (referred to as *S0*) passes nothing into the MA-Net processor since all its inputs are local whereas frameworks #2 and #3 (referred to as *SA* and *SS* hereafter) process and aggregate neighboring information and mix them with localized input before passing them to the processor.

As introduced earlier, C0 is the collection of all image patches whereas C1 only contains patches in C0 that have no less than 10 % pixels being water bodies. For each image patch in C0, the median DEM value among 65,536 (256 by 256) pixels will be used to represent the elevation of the whole patch. Then, for each patch in C1, we determine its contributing neighbors following the concept of k-th hop neighbors (Feng *et al.* 2022) of graphs. In short, the k-th hop neighbors have an exact distance/moves of k to the target node. In contrast, k-hop neighbors are the aggregation of i-th hop neighbors where $i \leq k$. Here, image patches are nodes and the distance between a node and any of its neighbors is defined as the number of steps needed according to the D8 flow direction algorithm to travel from any node to the target node. Figure 3 illustrates the how k-th hop neighbors of a target node are determined using the D8 algorithm.

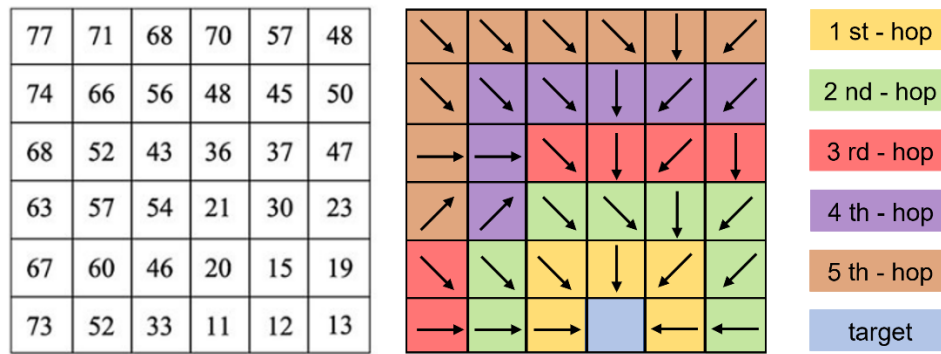


Figure 3. Patch-wise median elevation (left) and corresponding k-th hop neighbors following D8 flow directions.

In this study, we account for neighbors within five hops out of computational efficiency and practical considerations. Specifically, the fifth-hop neighbors of any target pixel can reach areas that are at least $5 \text{ (steps)} \times 256 \text{ (number of pixels for width or height of the patch)} \times 10 \text{ (spatial resolution)} = 12.8 \text{ km}$ away, assuming all steps toward the target patch are horizontal or vertical, which, we believe, provides a scope large enough for the target patch to draw information from. Once the neighbors are determined, for each neighbor of the current target, we create seven summary values (five for cumulative precipitation and two for soil moisture) using Eq.1:

$$v_L = \frac{1}{H \times W} \sum_{i=1}^H \sum_{j=1}^W L(i, j) \quad (1)$$

where L represents the cumulative precipitation layers or soil moisture feature layers for this patch, and H and W is the height and width of the patch. This process will be repeated for every neighboring patch of the target, which results in a $7 \times n$ (n is the number of neighbors) matrix that carries information from surrounding areas. A target patch could have a random number of neighbors, which can be a problem for most DL models, including those that are used in this

study, for DL models are usually able to deal with unified input only. Considering that, we further transform the $7 \times n$ matrix into a 7×20 one by averaging data coming from neighboring patches that are at the same distance to the target patch. Table 1 lists all possible distances between a target and its neighbors in the five-hop collection.

Table 1. All possible distances between a target and its neighbors within five hops

Hop	Distance Combinations ($\times 256 \times 10 m$)					
1 st	1	$\sqrt{2}$	-	-	-	-
2 nd	2	$1+\sqrt{2}$	$2 \times \sqrt{2}$	-	-	-
3 rd	3	$2+\sqrt{2}$	$1+2 \times \sqrt{2}$	$3 \times \sqrt{2}$	-	-
4 th	4	$3+\sqrt{2}$	$2+2 \times \sqrt{2}$	$1+3 \times \sqrt{2}$	$4 \times \sqrt{2}$	-
5 th	5	$4+\sqrt{2}$	$3+2 \times \sqrt{2}$	$2+3 \times \sqrt{2}$	$1+4 \times \sqrt{2}$	$5 \times \sqrt{2}$

The distances listed in Table 1 show how many diagonal and non-diagonal steps a neighbor patch can possibly take to reach the target regardless of the sequence. Note that we do not distinguish between $1+\sqrt{2}$ (a non-diagonal move followed by a diagonal move) and $\sqrt{2}+1$ (a diagonal move followed by a non-diagonal move). Then, data from patches with the same distances will be averaged. For instance, we create a 7×1 array by averaging the two yellow patches that travel diagonally in Figure 3 to represent data coming from neighbors at a $\sqrt{2}$ distance. Similarly, a separate 7×1 array will be used to store the averages for the remaining three yellow non-diagonal patches at a distance of 1. We repeat this process until all neighbors of the current patch are processed. If a target patch does not have neighbors at a certain distance, the corresponding 7×1 array will be filled with zeros. By aggregating information based on distance, we converted from the arbitrary-sized $7 \times n$ input matrix to a fixed size of 7×20 for any target patch.

We further found that some image patches in C1 do not have neighbors at all, which means, their status will not be affected by surrounding areas. Given that, we filter the patches in C1 to remove those that do not have any contributors around them based on hydrologic connectivity. This ensures every image patch that passes the screening has at least one contributor around it and can thus satisfy all three frameworks in Figure 2. We will refer to this collection as C2. As a result, C2 contains 8,932 256-by-256 image patches with 10 m spatial resolution and will be divided into training, validation, and test sets following a 7:2:1 ratio.

3.1.1. Design and Implementation of Frameworks SA and SS

For framework SA, we first fed the 7×20 matrix to a multi-layer perceptron (MLP) to make it a 7×1 array. For framework SS, the 7×20 matrix was transposed and treated as a sequence with 20 “words” where each word is represented by a vector (embedding) of 7. Next, we expanded the embedding length from 7 to 64 using a linear layer to make it compatible with the structure of a 1-layer, 8-head encoder structure of a Transformer. The encoder-only Transformer generated the

output for the “next time step” based on the input sequence, resulting in an 1×7 output vector. The vector was then transposed again into 7×1 . Next, for both SS and SA, the resulting 7×1 array was expanded into a $7 \times H \times W$ matrix to match the size of the localized input of the target location. Since the expansion process simply stretches the single pixel into a 2D plane of pixels with all pixels being the same, we applied a convolutional layer to the $7 \times H \times W$ matrix to introduce some differences into pixels on each $H \times W$ plane. Those pixel values were updated several times during the backward pass at the model’s training stage. Finally, we applied the Convolutional Block Attention Module (CBAM) to the resulting $7 \times H \times W$ matrix to make the model focus on features that were more channel-wisely relevant as well as on locations that were the most contributing to predictions. The resulting $7 \times H \times W$ matrix was then added to the five cumulative precipitation and two soil moisture layers of the localized input matrix, and the result was fed to the MA-Net processor. Figure 4 depicts the structure and dataflows of SA and SS frameworks.

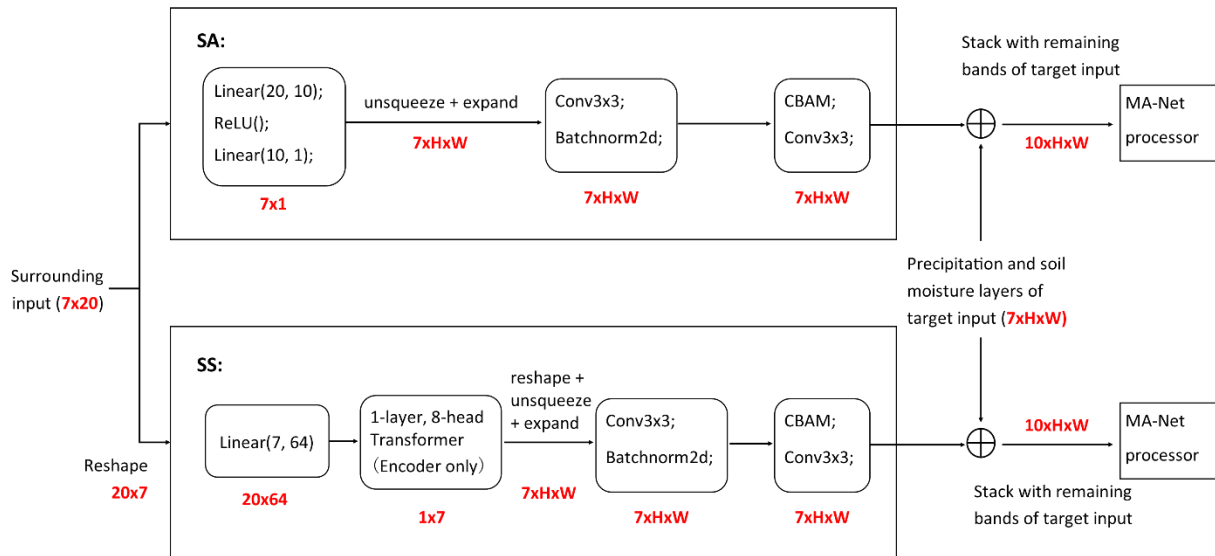


Figure 4. The structure of frameworks SA and SS, and the data processing with both frameworks. Text in red indicates the corresponding shape of data.

In summary, frameworks SA and SS both simulate the influences of surrounding information on the current location, but they differ from each other in how they handle those data. As explained above, SA aggregates data by using an MLP layer that does not distinguish between data at different distances. In contrast, SS is capable of taking into consideration both the data and the position where the data come from.

3.1.2. Explanation of Sub-Modules in Frameworks SS and SA

CBAM module is proposed by Woo *et al.* (2018) as a lightweight and general module working with convolutional layers to help the model concentrate on meaningful features along channel and spatial axes. In short, CBAM compresses pixel values on a $H \times W$ feature plane or along the

channel axis to a single value by taking the maximum or the average plane-wise or channel-wise. Then, it concatenates and/or adds those results and multiplies the resulting arrays to the original feature map to update original feature maps with global information. CBAM has been proven to improve CNN model performance in various tasks (Wang *et al.* 2019, Li *et al.* 2022b, Rajyalakshmi *et al.* 2022).

Transformer is an encoder-decoder structure introduced by Vaswani *et al.* (2017) to break the constraint of sequence models such as LSTM, GRU, and other Recurrent neural networks (RNN) structures. By replacing recurrence with a pure attention mechanism, Transformers process the entire sequence at the same time, which allows better parallelization inside hardware. Moreover, describing the location of every word in a sequence using positional encoding allows Transformers to get rid of the vanishing gradient issue that is common for most RNN models and therefore makes Transformers better at dealing with long sequences. In this study, we modified the Post-Layer Normalization (Post-LN) Transformer (Liu *et al.* 2020, Xiong *et al.* 2020) to fit our needs. As a major modification, the encoder-only structure was adopted as our task is a sequence-to-one prediction rather than sequence-to-sequence. In other words, we care about the present influence of neighbor input on the target location rather than focusing on how that result changes over time. For the second modification, layer normalization was removed. We adopt those modifications following findings from the work done by Castangia *et al.* (2023), for they reported better model performance and generalization capabilities with those modifications in a study of predicting water levels of Dobo station on Sava River one day ahead.

3.2. Model Understanding with Gradient-Based Explainable AI

Deep learning models have long been considered “black box” models (Dosilovic *et al.* 2018, Xu *et al.* 2019, Ekanayake *et al.* 2022) for their limited interpretability. Understanding how features are contributing to the output in a deep model is of great importance for not only improving the credibility of the result but acquiring new knowledge by understanding the causes and the phenomenon. In this study, we adopt a gradient-based method for model explanation. Gradient-based methods are based on the idea that gradients of the output with respect to the input define the importance or saliency of input for the output (Simonyan *et al.* 2014). The key steps of the XAI method used in this study can be summarized as 1) condense the output from a matrix to a scalar 2) compute the gradient of that scalar with respect to the input features; 3) average those gradients over the feature plane, average the results over all images in the test set, and then take the absolute value to obtain the saliency score for that specific feature.

Gradients are computed during the backward pass which requires a scalar as input. Given that we care more about pixels of which backscatter values will change during meteorological processes and those pixels are usually located around river channels (including their tributaries) and lake areas, the scalar will be computed using those pixels of interest. Eq. 2 describes the process:

$$sum_k = \sum_i \sum_j pred_{i,j}, if pred_{i,j} < Otsu(Pred_k) \quad (2)$$

$Pred_k$ is the $1 \times H \times W$ prediction matrix of the k-th image patch and $pred_{i,j}$ is the predicted backscatter at position (i, j) on the $H \times W$ plane. Otsu is a thresholding method that separates pixels into foreground and background by maximizing inter-class variance (Nobuyuki Otsu 1979). As water bodies usually appear darker on SAR images, predictions that are less than the threshold will be considered.

One thing that is worth mentioning about step #2 is the input for which we compute gradients. As discussed in 3.1.1, Only SA and SS take data from surrounding areas whereas all three models take localized input for the target location. To make gradients from different models comparable, we compute the gradients for the input matrix of the current location following step #3 defined by Eq. 3:

$$Grad_{local_c} = \frac{1}{H \times W} \sum_i \sum_j Grad_{i,j} \quad (3)$$

$Grad_{local_c}$ is the averaged saliency score for c-th feature of the input matrix of the target image patch and represents the importance of that specific feature to results (Selvaraju *et al.* 2020). Specifically, for each target image sample, $Grad_{local}$ is a 10-element array that corresponds to the 10-layer localized input matrix of the target location. The resulting gradient arrays will then be averaged over all samples/patches in the test set. Finally, we will take the absolute value for every element in the average array as the saliency scores.

3.3. Model Implementation

All three frameworks were implemented using PyTorch and trained on four Tesla K80 GPUs. We adopted an initial learning rate of $5e^{-3}$, a batch size of 64, and an Adam optimizer with β_1 being 0.9 and β_2 being 0.98. A learning rate scheduler was used to gradually decrease the learning rate when the performance plateaued. For SS, we also adopted a linear warmup stage during the first 50 epochs following conclusions of previous studies about Transformer (Popel and Bojar 2018, Liu *et al.* 2019) to stabilize training. S0, SA, and SS are all trained for 200 epochs with an early stop technique. We adopted the loss function used in the study done by Li *et al.* (2022c). It is calculated as Eq. 4:

$$LossFN = 0.5 \times MAE + 0.5 \times (1 - NSE) \quad (4)$$

MAE represents the mean absolute error (Eq. 5) and NSE represents Nash-Sutcliffe efficiency (Eq. 6), where $pred_i$ and obs_i are samples of model prediction and observation, respectively.

$$MAE = \frac{\sum_{i=1}^n |pred_i - obs_i|}{n} \quad (5)$$

$$NSE = 1 - \frac{\sum_{i=1}^n (pred_i - obs_i)^2}{\sum_{i=1}^n (obs_i - \overline{obs})^2} \quad (6)$$

Following the work MA-SARNet, we adopted Sinkhorn Divergence (SD) in addition to MAE and NSE to evaluate model performance. The Assemble Accuracy Index (AAI) will be built with a combination of MAE, NSE, and SD as computed in Eq. 7:

$$AAI = \frac{1}{1 + MAE} + \frac{1}{1 + SD} + NSE \quad (7)$$

We encourage readers to check the MA-SARNet paper for a detailed explanation of why AAI is needed and why it is created in the way shown in Eq. 7. In short, AAI not only unifies among different scales of its components but allows us to evaluate model performance from different perspectives in terms of the averaged model estimation error (Willmott and Matsuura 2005), the difference between probability distribution of predicted values and that of the ground truth (Oneto *et al.* 2020), and how well the predictions match observations (McCuen *et al.* 2006). In summary, MAE ($[0, +\infty)$) and SD ($[0, +\infty)$) can be treated as model errors and thus the lower they are the better the model performance is. In contrast, NSE ($(-\infty, 0]$) and AAI ($(-\infty, 3]$) are more about indicating accuracy, and we want them to be as high as possible.

4. Results and Discussions

4.1. Performance of Frameworks S0, SA, and SS

The benchmark performance is obtained with persistence assumptions. In other words, the backscatters captured one visit prior to the current observations will be treated as predictions for the present. Persistence is selected as the benchmark mainly because there are, so far, no process-based models that can translate directly meteorological processes and the influence of other relevant factors to surface backscatters such as SAR signals. In contrast, previous studies found the persistence powerful and robust enough to serve as benchmark in tasks including streamflow forecasting (Krajewski *et al.* 2021) and image synthesis (Diaconu *et al.* 2022; Guatam *et al.*, 2022). Table 2 listed the persistence benchmark and performance of S0, SA, and SS frameworks.

All three data-driven frameworks, regardless of whether it only considers localized input, generate more accurate predictions compared to the persistence benchmark. Remember MAE and SD are “errors” whereas NSE and AAI are “accuracy” terms. Table 2 clearly shows that all four indexes for S0, SA, and SS are improved compared to the benchmark. Table 2 also shows that considering precipitation and soil moisture information from surrounding areas further improved model performance, for SA and SS outperformed S0. SS and SA, however, were not significantly different from each other in terms of performance statistics shown above.

Table 2. Performance of frameworks S0, SA, and SS trained for 200 epochs compared with the persistence benchmark.

Model	Item	MAE Mean	MAE Median	SD Mean	SD Median	NSE Mean	NSE Median	AAI Mean	AAI Median
Benchmark	Statistics	2.21	1.97	1151.37	838.99	0.59	0.74	0.92	1.08
S0	Statistics	1.61	1.44	638.08	465.64	0.78	0.85	1.18	1.26
	Compared to Benchmark (%)	-27.15	-26.90	-44.58	-44.50	32.20	14.86	28.26	16.67
SA	Statistics	1.58	1.42	616.84	444.64	0.79	0.86	1.19	1.27
	Compared to S0 (%)	-1.86	-1.39	-3.33	-4.51	1.28	1.18	0.85	0.79
SS	Statistics	1.58	1.42	617.61	442.71	0.79	0.86	1.19	1.27
	Compared to S0 (%)	-1.86	-1.39	-3.21	-4.92	1.28	1.18	0.85	0.79

Figure 5 depicts the predicted backscatters from S0, SA, and SS, as well as the persistence benchmark and the target (ground truth) SAR image. The first thing we noticed is that S0, SA, and SS all managed to translate successfully from model input to target backscatters even if for scenes with complex geometry such as scenes #1 and #3. In addition, all three data-driven frameworks performed better in situations where the previous SAR differs noticeably from the current one, such as scene #2 and the location inside the red box of scene #1, thanks to being exposed to not only the previous SAR but many other relevant factors and driving forces. Similarly, we see examples where the diversity in input makes predictions less prone to noise contained in the previous SAR image, such as those spots shown in scene #4. Although the prediction quality is satisfying both visually and quantitatively, there are a few cases where the model’s decision was dominated by one or a few features and thus failed to present enough details in the output such as those in the red squares and triangles in scene #3. The land cover layer is highly likely to be the misleading factor in those cases.

Scene #4 is worth a bit more explanation. Normally, water bodies are darker than other land cover types on SAR images. However, there are chances for a small part of water bodies to appear super bright (as shown in scene #4) if it happened to be reflecting the energy in the direction the sensor is looking. Because those super bright spots are usually “fake” and do not refer to any real entities, it is, thus, helpful if the model can safely remove those fake features. We believe the removal of bright spots in scene #4 is safe because of the inconsistency between the previous and the target SAR images. There are bright spots on scenes #3 and #1 as well, but they are not removed as they are consistent among the previous and target images and therefore are more likely to be characteristics of real entities or structures on the ground. Those different behaviors indicate that our models can recognize fake features and take actions accordingly.

When comparing the first three columns of images, we do not see major differences overall but some small discrepancies locally such as shown in those yellow boxes in scenes #2 and #4.

Those discrepancies, without doubt, are because of the additional data coming from neighboring areas (S0 versus SA and SS) as well as the mechanism the data are utilized (SS versus SA). We will provide a detailed analysis of how these three frameworks pay attention to data fed to them in sub-section 4.3.

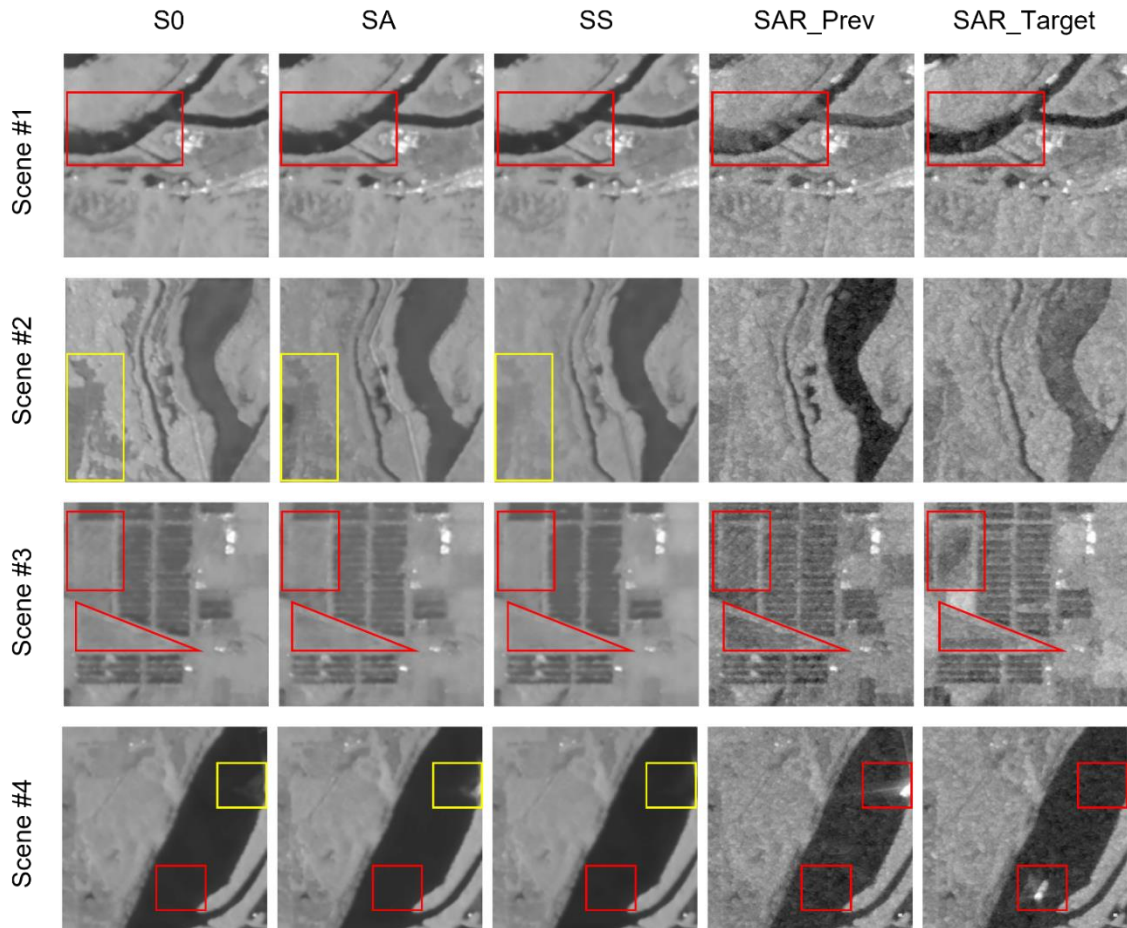


Figure 5. Predictions from S0, SA, SS as well as the persistence benchmark (SAR_Prev) and the target SAR image (SAR_Target)

4.2. Influence of Model Configurations on the Performance of SA and SS

Table 3 lists the performance of some model configurations we tested. SA_id1 and SS_id1 are configurations for which the performance is listed in Table 2 as SA and SS, respectively. SA_id2 concatenates the $7 \times H \times W$ input matrix from surrounding locations with the $10 \times H \times W$ input from the target location, instead of adding them to the corresponding layers of the target matrix. SS_id2 and SS_id3 both have a complete six-layer encoder-decoder structure compared to SS_id1 for which only a one-layer encoder exists. SS_id2 has a Pre-LN (Pre-Layer Normalization) structure for which layer normalization is applied before the multi-head attention process and then the attention matrix and residuals are added. In contrast, SS_id3 has a Post-LN structure where layer normalization is applied to the sum of the attention matrix and residuals.

We encourage readers to check the work done by Xiong *et al.* (2020) for a detailed comparison between Post-LN and Pre-LN Transformers.

Table 3. Performance of SS and SA frameworks with different model configurations

Model	Item	MAE	MAE	SD	SD	NSE	NSE	AAI	AAI
		Mean	Median	Mean	Median	Mean	Median	Mean	Median
SA	id1 statistics	1.58	1.42	616.84	444.64	0.79	0.86	1.19	1.27
	id1 against S0 (%)	-1.86	-1.39	-3.33	-4.51	1.28	1.18	0.85	0.79
	id2 against id1 (%)	0.63	<u>-0.70</u>	0.68	<u>-1.92</u>	0.00	0.00	0.00	0.00
	id2 against S0 (%)	-1.24	-2.08	-2.67	-6.34	1.28	1.18	0.85	0.79
SS	id1 statistics	1.58	1.42	617.61	442.71	0.79	0.86	1.19	1.27
	id1 against S0 (%)	-1.86	-1.39	-3.21	-4.92	1.28	1.18	0.85	0.79
	id2 against id1 (%)	1.27	<u>-0.70</u>	2.98	0.38	-1.27	0.00	-0.84	0.00
	id2 against S0 (%)	-0.62	-2.08	-0.32	-4.56	0.00	1.18	0.00	0.79
	id3 against id1 (%)	1.27	0.70	2.42	2.15	-1.27	-1.16	-0.84	0.00
	Id3 against S0 (%)	-0.62	-0.69	-0.87	-2.88	0.00	0.00	0.00	0.79

Table 3 clearly shows that model configurations have moderate impact on model performance. For instance, SA_id2 has slightly better median values for MAE and SD compared to SA_id1, and SS_id2 also has a higher median MAE over SS_id1 shown by the underlined figures in Table 3. Due to the complexity of deep learning models and the huge amount of hyperparameters to be tuned, it is very unlikely, if not impossible at all, for us to reach the global optimal setting. Nevertheless, according to the results, the additional data from neighboring areas are more important to model performance than model settings (e.g., concatenate versus adding and small changes in model structures). In other words, as long as the model configurations are reasonably determined, we will get a better result if we consider extra contributing data. In this study, we picked initial hyperparameters following general suggestions and training tips in the literature and then fine-tuned some of them in a trial-and-error manner. We believe, at least for this study, it will not be worth the time and resources needed to reach the optimal hyperparameter setting based on results of the sensitivity analysis.

To further understand the importance of data, we tested the performance in three cases (referred to as SA_id3, SA_id4, SA_id5) where all model configurations are the same while the input is different. Table 4 lists the performance of those tests as well as S0’s performance for comparison. Recall from what are discussed in sub-sections 3.1 and 3.1.1, originally, the cumulative precipitation and soil moisture features of each neighbor image patch will be averaged over the $H \times W$ plane, resulting in a 7×1 array carrying the summarized information of five rainfall plus two soil moisture conditions. Then, arrays coming from neighbors that have the same distance toward the target patch will be averaged again. For SA_id4 and SA_id5, we simply replace those two averaging steps by taking the maximum / sum.

Table 4. Performance of SA framework fed with three different data aggregation (all trained for 150 epochs)

Model	Aggregation Approach	MAE	MAE	SD	SD	NSE	NSE	AAI	AAI
		Mean	Median	Mean	Median	Mean	Median	Mean	Median
S0 statistics	-	1.61	1.44	638.08	465.64	0.78	0.85	1.18	1.26
SA_id3 against S0 (%)	Average	-1.24	-1.39	-3.00	-4.15	1.28	1.18	0.85	0.79
SA_id4 against S0 (%)	Maximum	-0.62	0.00	-1.26	-2.60	1.28	1.18	0.00	0.79
SA_id5 against S0 (%)	Sum	0.00	0.69	-0.50	-2.64	0.00	1.18	0.00	0.00

Table 4 shows that averaging is the best way of aggregating neighboring data in terms of model performance, followed by taking the maximum and then the sum. This is consistent with the common practice in the deep learning research field where the average and/or the maximum value over a feature plane is often used to provide a “global view” to help the model focus on important features and/or locations (Woo *et al.* 2018, Hu *et al.* 2020).

As we stressed the importance of data, one question that naturally arises is: why not take full advantage of data in surrounding areas by leveraging them at pixel level rather than doing aggregation? No aggregation will allow more data points and it is thus likely to further improve predictions. Unfortunately, there are three main difficulties preventing us from integrating data at a pixel level. First is the fundamental spatial assumption of CNN models. SA and SS process neighboring information in different ways, but both need to feed their results to MA-Net processor which is a CNN model. CNN models can process multiple feature layers stacked together with the input being a $N \times C \times H \times W$ matrix, where N is the batch size (number of image patches per batch), C is the number of feature layers, and H and W is the height and width of each feature layer. If we pick a pixel column at any location in a stacked feature map from a $1 \times C \times H \times W$ matrix, the resulting $1 \times C \times 1 \times 1$ pixels will precisely point to the same location. For instance, for an RGB image containing a cat, the location of the cat’s nose (or whatever entity) should be the same on the red, green, and blue feature layers of the image. Given that, if we are to mix input from neighbor areas and current location at a pixel level, theoretically, we should not add or concatenate them in the matrix form, as these two operations require pixels along the channel dimension to be from the same location. That means, to make those data work together, we still need to remove their spatial attributes somewhere before data from different areas are mixed.

In addition to the spatial assumption issue, the computation cost is another challenge that we can hardly get rid of right now. Theoretically, any target image patch can have up to 120 neighbors within the 5-hop distance. Given that, in addition to the $10 \times H \times W$ input matrix at the current location, we will need to go over the input matrix for surrounding areas that contains up to $120 \times 7 \times H \times W$ pixels to be able to forecast the backscatters for the current location. In the worst scenario, pixel-level data integration can lead to over 80 times more computation. In the best case where each target image only has one neighbor, about 70% additional computation

will still be required, even if we managed to find a way to resolve the spatial assumption issue mentioned above with no additional computation.

Finally, the pixel-level approach may cause problems in data processing and may lead to unstable training. Again, this is because target patches can have random numbers of neighbors, which may cause a problem for most deep learning models as they require unified input. For instance, a patch with one neighbor has a neighboring data matrix of shape $1 \times 7 \times H \times W$, whereas a patch with thirty neighbors has a $30 \times 7 \times H \times W$ neighboring data matrix. In practice, it is common to modify a small number of invalid values in feature maps (Che *et al.* 2018, Khan *et al.* 2022), but it remains unclear whether that approach works for cases where a majority pixels need to be changed, such as the example above.

Graph Neural Network (GNN) is a promising model structure for its better representation of graph-like data structures, such as river networks and weather stations (Sun *et al.* 2022), and thus may play a key role in solving those three issues discussed above. However, due to the complexity of those issues, more research is needed to improve the computational efficiency of GNN models as well as to equip them with more flexibility to better represent complex graph structures.

4.3. Understanding the Significance of Input Features with Gradient Analysis

Figure 6 depicts the saliency score of each feature in the localized input matrix. As mentioned in sub-section 3.2 each saliency score was obtained by averaging over all image samples in the test set. It is worth noticing that since the unit of gradients is [the unit of output] / [the unit of input], scores among different features are not comparable. In addition, those features that do have the same input unit, such as those precipitation and soil moisture layers, are still different scales from each other after standardization, making inter-feature comparisons not appropriate. Figure 6 clearly shows how different models pay “attention” to the same data they are fed with. Specifically, considering data from surrounding areas, regardless of whether the data was processed with SA or SS, improves the importance of HAND, precp4, and sm1. In contrast, if not provided with the additional data, the model will pay more attention to land cover, precp1~precp3, and the previous SAR image. The difference between SA and SS in terms of the feature importance of those five precipitation layers is complex to describe. Based on the charts below, SA values precp1 and precp5 more than SS does, whereas precp2 and precp4 are more important for SS than for SA. In addition to those, precp3 is comparably important to SS and SA. Apart from those precipitation layers, soil moisture information is valued more for SS and the attention of SA and SS on all the other features are quite similar.

The saliency score chart allows us a better understanding of the difference between predictions generated by S0, SA, and SS. As shown in those yellow boxes in scene #4 of Figure 5, SS is the least affected by the bright spot caused by a special reflecting angle on the previous SAR. This is because SS relies the least on the previous SAR among all three frameworks and meanwhile has a medium-level dependency on land cover. As we discussed in sub-section 4.1, as the bright spot is a coincidence that does not correspond to any real difference in surface

characteristics, it will not be recorded in other geomorphic feature layers, such as the land cover map. Thus, a higher attention on the land cover layer and a lower attention on the previous SAR could prevent the model from being adversely affected by misleading information on the latter. In contrast, although SA relies less on the previous SAR image compared to S0, its attention to land cover is insufficient, which therefore explains SA’s slightly worse performance inside the yellow box compared to S0.

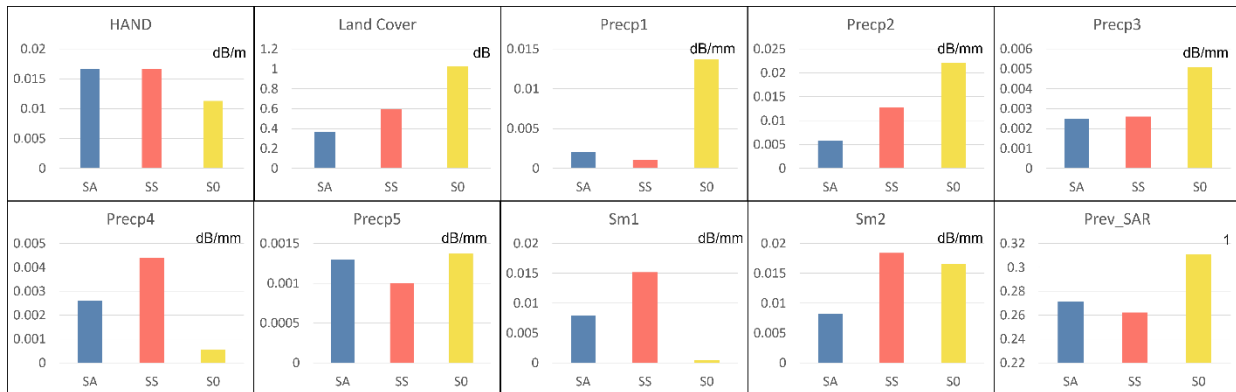


Figure 6. Saliency scores for each feature of the localized input matrix for S0, SA, and SS

5. Conclusion

In this study, we proposed two one-shot SAR nowcasting frameworks, SA and SS, that consider precipitation and soil moisture information from surrounding areas that contribute to the status of the target location. Our goal is to improve the existing localized one-shot model for Earth’s surface characteristics prediction by introducing more physical features and hydrological connections between adjacent areas. For any target location, the contributing neighbors are determined by the D8 flow direction algorithm. SA integrates surrounding information through spatial aggregation by applying an MLP layer to the result of a two-step averaging whereas SS treats the averaged information as a spatial series and generates the “next token” corresponding to the input token series using an encoder-only Transformer structure.

Predictions of backscatters of SAR images captured during 2019 Central US Flooding from SA, SS, and S0 (only considers input from the target location) were compared against the benchmark generated with the persistence assumption. Results show that all three forecast frameworks outperform the benchmark. A comparison among SA, SS, and S0 indicated that considering data coming from surrounding areas that contribute to the target location can further improve prediction accuracy. The median and mean of the four evaluation indexes for SA and SS did not noticeably differ from each other. Sensitivity analysis was conducted on SS and SA with different hyperparameters and with surrounding data generated by taking the average/maximum/sum. We found that data played a more dominant role than hyperparameters, as predictions were more sensitive to changes in data. We, therefore, suggest that more effort should be put into data collection and processing, as reasonably selected (e.g., by checking suggestions of previous studies in the literature) hyperparameters only result in small differences.

The XAI analysis clearly indicated the shift of the model's attention when extra information was provided. In addition to the influence of data, the way data was integrated also played a part in determining the importance of each input feature.

Due to the limited computation resources and existing model structures, right now, we cannot integrate surrounding data at the pixel level but can only do aggregation, such as taking the average/maximum/sum over a 2D feature plane, which is a waste of useful information. In addition, due to the data processing mechanism of the CNN model, we cannot integrate surrounding data while keeping the original shape, such as watershed boundaries, of the locations that provide those data. Those are potential directions for future work.

References

- Alabbad, Y., Yildirim, E. and Demir, I., 2022. Flood mitigation data analytics and decision support framework: Iowa Middle Cedar Watershed case study. *Science of The Total Environment*, 814, p.152768.
- Alabbad, Y. and Demir, I., 2022. Comprehensive flood vulnerability analysis in urban communities: Iowa case study. *International journal of disaster risk reduction*, 74, p.102955.
- Alparone, M., Nunziata, F., Estatico, C., Camps, A., Park, H., and Migliaccio, M., 2022. On the Trade-Off Between Enhancement of the Spatial Resolution and Noise Amplification in Conical-Scanning Microwave Radiometers. *IEEE Transactions on Geoscience and Remote Sensing*, 60.
- Ao, Z., Sun, Y., Pan, X., and Xin, Q., 2022. Deep Learning-Based Spatiotemporal Data Fusion Using a Patch-to-Pixel Mapping Strategy and Model Comparisons. *IEEE Transactions on Geoscience and Remote Sensing*, 60, 5407718.
- Aristizabal, F., Judge, J., and Monsivais-Huertero, A., 2020. High-resolution inundation mapping for heterogeneous land covers with synthetic aperture radar and terrain data. *Remote Sensing*, 12 (6), 900.
- Bosch, M., Conroy, C., Ortiz, B., and Bogden, P., 2020. Improving emergency response during hurricane season using computer vision. In: *Earth Resources and Environmental Remote Sensing/GIS Applications XI*. SPIE, 14.
- Castangia, M., Grajales, L.M.M., Aliberti, A., Rossi, C., Macii, A., Macii, E., and Patti, E., 2023. Transformer neural networks for interpretable flood forecasting. *Environmental Modelling & Software*, 160, 105581.
- Che, Z., Purushotham, S., Cho, K., Sontag, D., and Liu, Y., 2018. Recurrent Neural Networks for Multivariate Time Series with Missing Values. *Scientific Reports*, 8 (1), 1–12.
- Chen, G. and Wang, W.C., 2022. Short-Term Precipitation Prediction for Contiguous United States Using Deep Learning. *Geophysical Research Letters*, 49 (8), e2022GL097904.
- Chitwatkulsiri, D., Miyamoto, H., Irvine, K.N., Pilailar, S., and Loc, H.H., 2022. Development and Application of a Real-Time Flood Forecasting System (RTFlood System) in a Tropical Urban Area: A Case Study of Ramkhamhaeng Polder, Bangkok, Thailand. *Water (Switzerland)*, 14 (10), 1641.

- Czerkawski, M., Upadhyay, P., Davison, C., Werkmeister, A., Cardona, J., Atkinson, R., Michie, C., Andonovic, I., Macdonald, M., and Tachtatzis, C., 2022. Deep Internal Learning for Inpainting of Cloud-Affected Regions in Satellite Imagery. *Remote Sensing*, 14 (6), 1342.
- Demir, I., Conover, H., Krajewski, W.F., Seo, B.C., Goska, R., He, Y., McEniry, M.F., Graves, S.J. and Petersen, W., 2015. Data-enabled field experiment planning, management, and research using cyberinfrastructure. *Journal of Hydrometeorology*, 16(3), pp.1155-1170.
- Demir, I. and Szczepanek, R., 2017. Optimization of river network representation data models for web-based systems. *Earth and Space Science*, 4(6), pp.336-347.
- Diaconu, C.-A., Saha, S., Gunnemann, S., and Xiang Zhu, X., 2022. Understanding the Role of Weather Data for Earth Surface Forecasting using a ConvLSTM-based Model. 1361–1370.
- Dosilovic, F.K., Brcic, M., and Hlupic, N., 2018. Explainable artificial intelligence: A survey. *In: 2018 41st International Convention on Information and Communication Technology, Electronics and Microelectronics, MIPRO 2018 - Proceedings*. Institute of Electrical and Electronics Engineers Inc., 210–215.
- Ekanayake, I.U., Meddage, D.P.P., and Rathnayake, U., 2022. A novel approach to explain the black-box nature of machine learning in compressive strength predictions of concrete using Shapley additive explanations (SHAP). *Case Studies in Construction Materials*, 16, e01059.
- Fan, T., Wang, G., Li, Y., and Wang, H., 2020. Ma-net: A multi-scale attention network for liver and tumor segmentation. *IEEE Access*, 8, 179656–179665.
- Fang, Z., Wang, Y., Peng, L., and Hong, H., 2021. Predicting flood susceptibility using LSTM neural networks. *Journal of Hydrology*, 594, 125734.
- Feng, J., Chen, Y., Li, F., Sarkar, A., and Zhang, M., 2022. How Powerful are K-hop Message Passing Graph Neural Networks. arXiv, <https://doi.org/10.48550/arXiv.2205.13328>
- Flanagan, P.X., Mahmood, R., Umphlett, N.A., Haacker, E., Ray, C., Sorensen, W., Shulski, M., Stiles, C.J., Pearson, D., and Fajman, P., 2020. A Hydrometeorological Assessment of the Historic 2019 Flood of Nebraska, Iowa, and South Dakota. *Bulletin of the American Meteorological Society*, 101 (6), E817–E829.
- Gautam, A., Sit, M. and Demir, I., 2022. Realistic river image synthesis using deep generative adversarial networks. *Frontiers in water*, 4, p.10.
- Guo, Z., Moosavi, V., and Leitão, J.P., 2022. Data-driven rapid flood prediction mapping with catchment generalizability. *Journal of Hydrology*, 609.
- Haltas, I., Yildirim, E., Oztas, F. and Demir, I., 2021. A comprehensive flood event specification and inventory: 1930–2020 Turkey case study. *International Journal of Disaster Risk Reduction*, 56, p.102086.
- Harris, L., McRae, A.T.T., Chantry, M., Dueben, P.D., and Palmer, T.N., 2022. A Generative Deep Learning Approach to Stochastic Downscaling of Precipitation Forecasts. *Journal of Advances in Modeling Earth Systems*, 14 (10), e2022MS003120.
- Hu, J., Shen, L., Albanie, S., Sun, G., and Wu, E., 2020. Squeeze-and-Excitation Networks. *IEEE Transactions on Pattern Analysis and Machine Intelligence*, 42 (8), 2011–2023.
- Hu, A. and Demir, I., 2021. Real-time flood mapping on client-side web systems using hand

- model. *Hydrology*, 8(2), p.65.
- Khan, H., Wang, X., and Liu, H., 2022. Handling missing data through deep convolutional neural network. *Information Sciences*, 595, 278–293.
- Kong, Y., Liu, S., and Peng, X., 2022. Multi-Scale translation method from SAR to optical remote sensing images based on conditional generative adversarial network. *International Journal of Remote Sensing*, 43 (8), 2837–2860.
- Krajewski, W.F., Ghimire, G.R., Demir, I., and Mantilla, R., 2021. Real-time streamflow forecasting: AI vs. Hydrologic insights. *Journal of Hydrology X*, 13, 100110.
- Kseňak, L., Pukanská, K., Bartoš, K., and Blišťan, P., 2022. Assessment of the Usability of SAR and Optical Satellite Data for Monitoring Spatio-Temporal Changes in Surface Water: Bodrog River Case Study. *Water (Switzerland)*, 14 (3), 299.
- Li, J., Xu, C., Su, H., Gao, L., and Wang, T., 2022a. Deep Learning for SAR Ship Detection: Past, Present and Future. *Remote Sensing*.
- Li, W., Wu, J., Chen, H., Wang, Y., Jia, Y., and Gui, G., 2022b. UNet Combined with Attention Mechanism Method for Extracting Flood Submerged Range. *IEEE Journal of Selected Topics in Applied Earth Observations and Remote Sensing*, 15, 6588–6597.
- Li, Z. and Demir, I., 2022. A comprehensive web-based system for flood inundation map generation and comparative analysis based on height above nearest drainage. *Science of The Total Environment*, 828, 154420.
- Li, Z., and Demir, I., 2023. U-net-based semantic classification for flood extent extraction using SAR imagery and GEE platform: A case study for 2019 central US flooding. *Science of The Total Environment*, 869, p.161757.
- Li, Z., Xiang, Z., Demiray, B.Z., Sit, M., and Demir, I., 2022c. MA-SARNet: A One-Shot Forecasting Framework for SAR Image Prediction with Physical Driving Forces. EarthArxiv, 4846, <https://doi.org/10.31223/X5765J>
- Li, Z., Mount, J. and Demir, I., 2022d. Accounting for uncertainty in real-time flood inundation mapping using HAND model: Iowa case study. *Natural Hazards*, 112(1), pp.977-1004.
- Liu, L., Jiang, H., He, P., Chen, W., Liu, X., Gao, J., and Han, J., 2019. On the Variance of the Adaptive Learning Rate and Beyond. arXiv, <https://doi.org/10.48550/arXiv.1908.03265>
- Liu, L., Liu, X., Gao, J., Chen, W., and Han, J., 2020. Understanding the difficulty of training transformers. In: *EMNLP 2020 - 2020 Conference on Empirical Methods in Natural Language Processing, Proceedings of the Conference*. 5747–5763.
- Liu, Y.Y., Maidment, D.R., Tarboton, D.G., Zheng, X., Yildirim, A., Sazib, N.S., and Wang, S., 2016. A CyberGIS Approach to Generating High-resolution Height Above Nearest Drainage (HAND) Raster for National Flood Mapping. *The Third International Conference on CyberGIS and Geospatial Data Science*, (August), 1–5.
- Markert, K.N., Markert, A.M., Mayer, T., Nauman, C., Haag, A., Poortinga, A., Bhandari, B., Thwal, N.S., Kunlamai, T., Chishtie, F., Kwant, M., Phongsapan, K., Clinton, N., Towashiraporn, P., and Saah, D., 2020. Comparing Sentinel-1 Surface Water Mapping Algorithms and Radiometric Terrain Correction Processing in Southeast Asia Utilizing

- Google Earth Engine. *Remote Sensing* 2020, Vol. 12, Page 2469, 12 (15), 2469.
- McCuen, R.H., Knight, Z., and Cutter, A.G., 2006. Evaluation of the Nash–Sutcliffe Efficiency Index. *Journal of Hydrologic Engineering*, 11 (6), 597–602.
- Nobuyuki Otsu, 1979. A Threshold Selection Method from Gray-Level Histograms. *IEEE Trans. Syst. Man Cybern*, 9 (1), 62–66.
- Oneto, L., Donini, M., Luise, G., Ciliberto, C., Maurer, A., and Pontil, M., 2020. Exploiting MMD and Sinkhorn Divergences for Fair and Transferable Representation Learning. *Advances in Neural Information Processing Systems*, 33, 15360–15370.
- Piadeh, F., Behzadian, K., and Alani, A.M., 2022. A critical review of real-time modelling of flood forecasting in urban drainage systems. *Journal of Hydrology*, 607, 127476.
- Popel, M. and Bojar, O., 2018. Training Tips for the Transformer Model. *The Prague Bulletin of Mathematical Linguistics*, 110 (1), 43–70.
- Rajyalakshmi, C., Rao, K.R.M., and Rao, R.R., 2022. A Novel Architecture Implementation Using Multi Scale Shared Residual Network from Remote Sensing Images for Extracting Water Bodies. *Ingenierie des Systemes d'Information*, 27 (2), 285–291.
- Requena-Mesa, C., Benson, V., Reichstein, M., Runge, J., and Denzler, J., 2021. EarthNet2021: A large-scale dataset and challenge for earth surface forecasting as a guided video prediction task. *In: IEEE Computer Society Conference on Computer Vision and Pattern Recognition Workshops*. 1132–1142.
- Salehi, B., Mahdianpari, M., Amani, M., M. Manesh, F., Granger, J., Mahdavi, S., and Brisco, B., 2018. A Collection of Novel Algorithms for Wetland Classification with SAR and Optical Data. *In: Wetlands Management - Assessing Risk and Sustainable Solutions*.
- Selvaraju, R.R., Cogswell, M., Das, A., Vedantam, R., Parikh, D., and Batra, D., 2020. Grad-CAM: Visual Explanations from Deep Networks via Gradient-Based Localization. *International Journal of Computer Vision*, 128 (2), 336–359.
- Simonyan, K., Vedaldi, A., and Zisserman, A., 2014. Deep inside convolutional networks: Visualising image classification models and saliency maps. *In: 2nd International Conference on Learning Representations, ICLR 2014 - Workshop Track Proceedings*.
- Sit, M.A., Seo, B. and Demir, I., 2023a. TempNet–temporal super-resolution of radar rainfall products with residual CNNs. *Journal of hydroinformatics*, 25(2), pp.552-566.
- Sit, M., Demiray, B.Z. and Demir, I., 2023b. Spatial Downscaling of Streamflow Data with Attention Based Spatio-Temporal Graph Convolutional Networks. *EarthArxiv*, 5227, <https://doi.org/10.31223/X5666M>
- Sit, M., Seo, B.C., Demiray, B.Z. and Demir, I., 2023c. EfficientRainNet: Smaller Neural Networks Based on EfficientNetV2 for Rainfall Nowcasting. *EarthArxiv*, 5232, <https://doi.org/10.31223/X5VQ1S>
- Sun, A.Y., Jiang, P., Yang, Z.L., Xie, Y., and Chen, X., 2022. A graph neural network (GNN) approach to basin-scale river network learning: the role of physics-based connectivity and data fusion. *Hydrology and Earth System Sciences*, 26 (19), 5163–5184.
- Tiwari, V., Kumar, V., Matin, M.A., Thapa, A., Ellenburg, W.L., Gupta, N., and Thapa, S.,

2020. Flood inundation mapping- Kerala 2018; Harnessing the power of SAR, automatic threshold detection method and Google Earth Engine. *PLOS ONE*, 15 (8), e0237324.
- Tuyen, D.N., Tuan, T.M., Le, X.H., Tung, N.T., Chau, T.K., Van Hai, P., Gerogiannis, V.C., and Son, L.H., 2022. RainPredRNN: A New Approach for Precipitation Nowcasting with Weather Radar Echo Images Based on Deep Learning. *Axioms*, 11 (3), 107.
- Twele, A., Cao, W., Plank, S., and Martinis, S., 2016. Sentinel-1-based flood mapping: a fully automated processing chain. *International Journal of Remote Sensing*, 37 (13), 2990–3004.
- Vandal, T.J., McDuff, D., Wang, W., Duffy, K., Michaelis, A., and Nemani, R.R., 2022. Spectral Synthesis for Geostationary Satellite-to-Satellite Translation. *IEEE Transactions on Geoscience and Remote Sensing*, 60.
- Vaswani, A., Shazeer, N., Parmar, N., Uszkoreit, J., Jones, L., Gomez, A.N., Kaiser, Ł., and Polosukhin, I., 2017. Attention is all you need. In: *Advances in Neural Information Processing Systems*. 5999–6009.
- Wang, D., Gao, F., Dong, J., and Wang, S., 2019. Change Detection in Synthetic Aperture Radar Images based on Convolutional Block Attention Module. In: *2019 10th International Workshop on the Analysis of Multitemporal Remote Sensing Images, MultiTemp 2019*. Institute of Electrical and Electronics Engineers Inc.
- Willmott, C.J. and Matsuura, K., 2005. Advantages of the mean absolute error (MAE) over the root mean square error (RMSE) in assessing average model performance. *Climate Research*, 30 (1), 79–82.
- Woo, S., Park, J., Lee, J.Y., and Kweon, I.S., 2018. CBAM: Convolutional block attention module. In: *Lecture Notes in Computer Science (including subseries Lecture Notes in Artificial Intelligence and Lecture Notes in Bioinformatics)*. 3–19.
- Xiong, R., Yang, Y., He, D., Zheng, K., Zheng, S., Xing, C., Zhang, H., Lan, Y., Wang, L., and Liu, T.Y., 2020. On layer normalization in the transformer architecture. In: *37th International Conference on Machine Learning, ICML 2020*. 10455–10464.
- Xu, F., Uszkoreit, H., Du, Y., Fan, W., Zhao, D., and Zhu, J., 2019. Explainable AI: A Brief Survey on History, Research Areas, Approaches and Challenges. In: *Lecture Notes in Computer Science (including subseries Lecture Notes in Artificial Intelligence and Lecture Notes in Bioinformatics)*. Springer, 563–574.
- Yang, M., Guo, C., Zhong, H., and Yin, H., 2020. A Curvature-Based Saliency Method for Ship Detection in SAR Images. *IEEE Geoscience and Remote Sensing Letters*, 18 (9), 1590–1594.
- Yildirim, E. and Demir, I., 2022. Agricultural flood vulnerability assessment and risk quantification in Iowa. *Science of The Total Environment*, 826, p.154165.
- Zanaga, D., Van De Kerchove, R., De Keersmaecker, W., Souverijns, N., Brockmann, C., Quast, R., Wevers, J., Grosu, A., Paccini, A., Vergnaud, S., Cartus, O., Santoro, M., Fritz, S., Georgieva, I., Lesiv, M., Carter, S., Herold, M., Linlin, L., Tsendbazar, N., Raimoino, F., and Arino, O., 2021. ESA WorldCover 10 m 2020 v100. *Meteosat Second Generation Evapotranspiration (MET)*, 1–27.
- Zhang, W., Hu, B., and Brown, G.S., 2020. Automatic surface water mapping using polarimetric

SAR data for long-term change detection. *Water (Switzerland)*, 12 (3), 872.

Zhu, J. and Kelly, T., 2021. Seamless Satellite-image Synthesis. *Computer Graphics Forum*, 40 (7), 193–204.